radiation

MDPI

Article

Impact of Microdosimetric Modeling on Computation of Relative Biological Effectiveness for Carbon Ion Radiotherapy

Shannon Hartzell [1,*], Keith M. Furutani [1], Alessio Parisi [1], Tatsuhiko Sato [2,3], Yuki Kase [4], Christian Deglow [5], Thomas Friedrich [5] and Chris J. Beltran [1]

[1] Department of Radiation Oncology, Mayo Clinic, Jacksonville, FL 32224, USA; furutani.keith@mayo.edu (K.M.F.); parisi.alessio@mayo.edu (A.P.); beltran.chris@mayo.edu (C.J.B.)
[2] Nuclear Science and Engineering Center, Japan Atomic Energy Agency, Tokai 319-1195, Japan; sato.tatsuhiko@jaea.go.jp
[3] Research Center for Nuclear Physics, Osaka University, Suita 567-0047, Japan
[4] B Dot Medical Inc., Edogawa-ku 143-0003, Japan; yuki.kase@bdotmed.co.jp
[5] GSI Helmholtzzentrum für Schwerionenforschung GmbH, 64291 Darmstadt, Germany; c.deglow@gsi.de (C.D.); t.friedrich@gsi.de (T.F.)
* Correspondence: hartzell.shannon@mayo.edu

Simple Summary: Modeling energy deposition on a microscopic scale is a useful tool for predicting biological outcomes in carbon ion radiotherapy. This study investigates how different approaches to calculating microdosimetric energy deposition influence predictions of biological effectiveness, which impact delivered patient doses. We compared several established models, along with a novel implementation that enables consistent geometrical comparisons among calculation approaches. Our results show that the choice of microdosimetric model can notably affect the calculated biological effectiveness. These results highlight the need to explicitly consider both the computational method and the assumed target geometry to ensure consistent and biologically meaningful predictions in particle therapy.

Abstract: Microdosimetry plays a critical role in particle therapy by quantifying energy deposition within microscopic domains to assess biological effects. This study evaluates the influence of different microdosimetric functions (MFs) and domain geometries (DGs) on relative biological effectiveness (RBE) predictions in carbon ion radiotherapy. Specifically, we compare the analytical microdosimetric function (AMF), calculated for spherical domains and implemented in PHITS, with the Kiefer–Chatterjee (KC) track structure model, which is conventionally applied to cylindrical geometries. To enable a direct comparison, we also introduce a novel implementation of the KC model for spherical domains. Using both models, specific energy distributions were calculated across a range of domain sizes and geometries. These distributions were input into the modified microdosimetric kinetic model (mMKM) to calculate RBE for the HSG cell line and compared against published in vitro data. The results show that both microdosimetric function and domain geometry significantly affect microdosimetric spectra and the resulting RBE, with deviations exceeding 10% when fixed mMKM parameters are used. Parameter optimization within the mMKM enables alignment across models. Our findings emphasize that microdosimetric function and domain geometry selection must be explicitly accounted for in microdosimetry-based RBE modeling, and that model parameters must be tuned accordingly to ensure consistent and biologically accurate predictions.

Keywords: microdosimetry; relative biological effectiveness; carbon ion radiotherapy; microdosimetric kinetic model; modified MKM; Kiefer–Chatterjee; particle therapy

check for updates

Academic Editor: Brigitta G. Baumert

Received: 17 April 2025
Revised: 8 June 2025
Accepted: 9 June 2025
Published: 12 June 2025

Citation: Hartzell, S.; Furutani, K.M.; Parisi, A.; Sato, T.; Kase, Y.; Deglow, C.; Friedrich, T.; Beltran, C.J. Impact of Microdosimetric Modeling on Computation of Relative Biological Effectiveness for Carbon Ion Radiotherapy. *Radiation* **2025**, *5*, 21. https://doi.org/10.3390/radiation5020021

Copyright: © 2025 by the authors. Licensee MDPI, Basel, Switzerland. This article is an open access article distributed under the terms and conditions of the Creative Commons Attribution (CC BY) license (https://creativecommons.org/licenses/by/4.0/).

1. Introduction

Carbon Ion Radiation Therapy (CIRT) relies on biophysical models to quantify radiation effectiveness, which can depend on both dosimetric and microdosimetric inputs specific to the patient's treatment plan. Microdosimetry, which assesses the spatial distribution of energy deposition at microscopic levels, is useful for predicting the relative biological effectiveness (RBE) of heavy ion radiation like carbon and is an integral component of some RBE models [1–3]. It links microscopic track structure to macroscopic dose distribution and helps to optimize biological dose delivery by maximizing tumor exposure while minimizing damage to healthy tissue [4].

Microdosimetric calculations involve defining a target domain such as a cell nucleus or a subnuclear structure, where individual energy depositions in the domain are typically presented as frequency and dose-weighted distributions of the microdosimetric quantities specific energy or lineal energy [1,2]. These microdosimetric distributions can be experimentally measured, modeled using computationally expensive Monte Carlo simulations [5–7], or derived from empirical or semi-empirical approaches. They can then be used as inputs in radiobiological model calculations of RBE and other related quantities [8–10]. This study will consider two common approaches to calculating microdosimetric spectra, namely the analytical microdosimetric function (AMF) [11,12], and the Kiefer–Chatterjee (KC) track structure model [13,14]. In this work, the KC model is implemented within a microdosimetric formalism and referred to as a distinct microdosimetric function for convenience. These two approaches are traditionally used in combination with different radiobiological models: the AMF is used in conjunction with the Mayo Clinic Florida microdosimetric kinetic model [15], while the KC model forms the original basis of the modified microdosimetric kinetic model (mMKM) [10,16].

The KC model is a pioneering track structure model that was used for the original biological dose calculations using the mMKM at NIRS/QST in support of CIRT, a foundation upon which the majority of modern clinical data was gathered [16,17]. In the NIRS/QST implementation, the KC model was applied using a cylindrical domain geometry as an approximation of the spherical geometry of a cell nucleus, as described by Kase et al. [16,17]. In contrast, the AMF [11,12], which has been implemented in the Particle and Heavy Ion Transport code System (PHITS) [18], calculates microdosimetric spectra for spherical water domains. The AMF was developed by fitting the results of detailed track structure simulations [19], which represents its most significant distinction from and potential refinement over the KC. The Mayo Clinic Florida microdosimetric kinetic model relies on the AMF, and therefore spherical domains, while the mMKM relies on the KC implemented for cylindrical domains.

This study aims to evaluate the sensitivity of microdosimetric spectra to calculation method, including the AMF and the KC model implemented as a microdosimetric function, and to variations in domain geometry. A key component is the novel implementation of the KC track structure model for spherical domains, which enables direct comparisons with the AMF under identical geometrical conditions. Furthermore, this study examines the effects of different microdosimetric calculation approaches on RBE predictions for CIRT within the mMKM framework. Particularly, it explores the necessary adjustments to mMKM parameters to accommodate changes in calculation methods while maintaining consistent RBE predictions.

2. Materials and Methods

2.1. Study Overview

The description of RBE calculation for CIRT using mMKM is well described in the literature and is summarized in Figure 1 [4,10,16]. The input required for the microdosi-

metric function includes both ion and microdosimetric domain parameters. Once selected, these inputs are used to compute the microdosimetric spectra, the methodology of which varies both by microdosimetric function and domain geometry. These microdosimetric spectra for the ion and the cell-specific parameters are then used to derive a deterministic microdosimetric quantity such as saturation-corrected lineal or specific energy (y_D^* or z_D^*, respectively). This quantity, along with the additional reference cell and radiation-specific parameters, is fed into the RBE model. In this example, the RBE model is mMKM, the output of which includes computational radiobiological quantities, such as RBE and RBE-weighted dose.

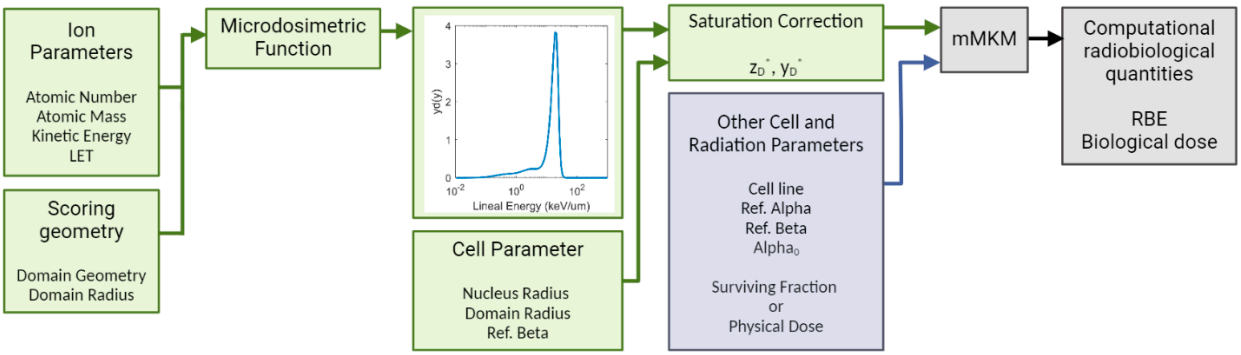


Figure 1. Schematic of the calculation of RBE by the mMKM.

In this study, we calculated the mMKM-based RBE (RBE_{mMKM}) using both the older (2006) and newer (2023) versions of the AMF for spherical domains, along with the KC model implemented for both cylindrical and spherical domains. Detailed implementations of each model are provided in subsequent sections. For each calculation method, we computed the microdosimetric spectra and deterministic microdosimetric quantities across a range of carbon energy spaced on a log scale from 1 to 900 MeV/u, corresponding to an LET range of 700 to 8 keV/µm. The ion stopping powers in water were taken from ICRU Reports 73 and 90 [20,21].

For RBE comparisons, a cylindrical domain radius of 0.32 µm was employed, aligning with cell characterizations in prior research [17,22]. To ensure volumetric equivalence between spherical and cylindrical domains, important because specific energy is defined as energy deposited per unit volume for an approximately consistent density, we calculated the spherical radius using

$$r_{sph} = \sqrt[3]{\frac{3{r_{cyl}}^3}{2}}. \quad (1)$$

This was derived under the assumption that the cylinder height equaled twice its radius, consistent with previous work [16,17]. For the selected cylindrical radius of 0.32 µm, this yields an equivalent spherical radius of 0.37 µm.

Additionally, we compared the effect of varying domain size on microdosimetric spectra for each calculation approach. For this comparison, cylindrical domain radii of 0.050, 0.10, 0.50, 1.0, and 5.0 µm were analyzed, along with corresponding spherical radii of 0.057, 0.11, 0.57, 1.1, and 5.7 µm to maintain volume equivalence across domain geometries.

2.2. Microdosimetry

In microdosimetry, specific energy (z) is a critical parameter that quantifies the energy deposited by a primary particle and all its secondaries in a domain per unit mass of the domain, typically expressed in Gy. Microdosimetric analysis involves frequency-weighted and dose-weighted probability distributions of the specific energy. The frequency-weighted spectra, $f(z)$, show the frequency of various specific energy events. Dose-weighted spectra,

$d(z)$, focus on the contribution of these events to the total absorbed dose, emphasizing which are most impactful for the tissue. These distributions are crucial for understanding the biological effects of radiation, as they describe the variability of energy deposition within microscopic targets.

2.2.1. AMF

We computed the microdosimetric spectra using the original AMF developed in 2006 [11] for use in the Japanese Monte Carlo system PHITS [18] and its improved version that was published in 2023 [12]. The AMF represents a fit to detailed track structure data and uses efficient analytical algorithms to model microdosimetric quantities in water by calculating the spatial coordinates of each ionization event and evaluating the probability densities of the number of ionization events within spherical target sites ranging from 3 nm to 1 µm in diameter [12]. The 2023 AMF [12] incorporates amendments based on updated track structure simulations with PHITS [18]. A detailed comparison between the results of the older and newer versions of the AMF can be found elsewhere [23]. This AMF can directly compute the frequency- and dose-weighted microdosimetric spectra for an ion given its given atomic number, atomic mass, kinetic energy, and LET.

2.2.2. KC Track Structure Model

The KC model is an amorphous track structure model that approximates the energy deposited in a microscopic domain. It combines the Kiefer model to represent the low-dose penumbra region and the Chatterjee model to describe the high-dose core region characteristic of charged particle tracks [13,14]. The KC model has historically been implemented using a cylindrical domain geometry to mimic a spherical cellular geometry in important studies supporting CIRT by Kase et al. and Inaniwa et al. [16,17].

In the KC model, the dose deposited at a radial distance R_i from the ion's path is given by

$$D_i = \begin{cases} \frac{0.000125 \cdot Z^{*2}}{{R_i}^2 \beta^2} = \frac{k_p}{{R_i}^2}, & R_c < R_i \leq R_p \\ \left(\frac{1}{\pi {R_c}^2}\right) \cdot \left(\frac{LET \cdot 0.1602}{\rho} - 2\pi k_p \ln\left(\frac{R_p}{R_c}\right)\right), & R_i \leq R_c \end{cases}, \quad (2)$$

where R_c and R_p describe the core and penumbra radii, respectively. Here, ρ represents the density of the domain (fixed at 1 g/cm^3 in this work), Z^* is the effective charge of the ion (calculated with the Barkas expression to account for the gradual electrical neutralization of ions at low velocity [24]), and β is the ion velocity relative to the speed of light. LET is provided in keV/µm, and all radii are provided in micrometers. The core and penumbra radii are determined by

$$R_c = 0.0116\beta \quad (3)$$

and

$$R_p = 0.0616\left(\frac{E}{A}\right)^{1.7}, \quad (4)$$

where E is the kinetic energy of the ion and A the atomic mass.

To compute specific energy for the cylindrical domain, energy deposition was calculated across 500 concentric annuli centered on the particle track, capturing contributions from both the core and penumbra regions. The full calculation details for this implementation can be found in Appendix A.1. For the spherical domain, the domain was treated as a series of thin cylindrical slices with varying radii stacked along the z-axis, with the same radial dose integration method applied to each slice (Appendix A.2).

For both geometries, energy deposition was calculated as a function of the impact parameter, defined as the perpendicular distance from the particle track to the center of the

domain (Appendix A.3). These spatially dependent energy depositions were then used to derive deterministic microdosimetric parameters, such as specific energy and lineal energy distributions (Appendix A.4).

2.3. RBE Calculation

The output of each microdosimetric function was used as input to the mMKM, which was proposed by Kase et al. as an adaptation to the original MKM to calculate RBE [10]. To calculate RBE_{mMKM}, the saturation-corrected dose-mean specific energy, z_D^*, was first calculated using microdosimetric spectra and cell specific parameters, including the domain radius (r_D) and nuclear radius (R_n), for each microdosimetric function (further described in Appendix A.4). This biologically corrected parameter was then combined with the alpha value in the case of LET approaching zero (α_0) to calculate α_{mMKM}. Therefore, for a fixed set of reference parameters (α_x and β_x), RBE_{mMKM} can be expressed as a function of microdosimetric function (*MF*), domain geometry (*DG*), and cell-specific parameters: $RBE_{mMKM}(MF, DG, r_D, R_n, \alpha_0)$.

For our RBE calculations, we adopted model parameters established by Inaniwa et al. in 2010 [16], which provided the best description of in vitro RBE data for human salivary gland (HSG) tumor cells irradiated with carbon ions [25]: RBE_{mMKM}(KC, CYL, 0.32 μm, 3.9 μm, 0.172 Gy^{-1}). To ensure volumetric equivalence, we employed r_D = 0.37 μm for spherical domains. The RBE_{mMKM} was calculated for a surviving fraction of 10% ($RBE_{10\%}$), for a carbon absorbed dose of 2 Gy (RBE_{2Gy}), and at low-doses (RBE_α), using previously established methods [15,26] and reference values of α_x= 0.313 Gy^{-1} and β_x= 0.0615 Gy^{-2} derived for HSG cells exposed to 200 kVp x-rays. RBE_{mMKM} predictions were compared with in vitro data measured by Furusawa et al. [25]. Using the same reference parameters fit by Inaniwa et al. for carbon ions [16], we additionally calculated RBE_{mMKM} using each of the microdosimetric functions for both helium and neon ions and further compared these calculations with in vitro data.

To additionally explore the impact of microdosimetric function on deterministic microdosimetric parameters and predictions of RBE_{mMKM} for various ions of the same LET, the parameter calculations were performed for protons, helium, and carbon ions at an LET of 9.9 keV/μm. In a further assessment for carbon ions, we then explored whether the RBE_{mMKM} calculated using different microdosimetric functions could approximate the KC cylinder model, selected as a reference due to its extensive use in clinical and computational studies [16,17,27], by optimizing the r_D, R_n, and α_0 parameters:

$$\min_{r_D, R_n, \alpha_0} \| RBE_{mMKM}(MF, DG, r_D, R_n, \alpha_0) - RBE_{mMKM}\left(KC, CYL, 0.32\ \mu m, 3.9\ \mu m, 0.172\ Gy^{-1}\right) \|^2 \quad (5)$$

3. Results

3.1. Impact Parameter and Microdosimetric Spectra

As part of the validation of our KC model implementation, we calculated specific energy as a function of impact parameter for both cylindrical and spherical domains of equivalent volume. These results are presented in Figure A7. The KC model results for the cylindrical domain reproduce those reported by Inaniwa et al. [16], confirming the accuracy of our implementation. Additionally, this work provides the first direct comparison of KC model predictions for spherical versus cylindrical geometries. At small impact parameters, the spherical domain yields higher specific energy, attributable to the longer path length of the particle track through the center of the sphere. This comparison highlights the influence of domain geometry on microdosimetric outcomes within the KC framework.

Figure 2 displays the frequency- and dose-weighted distributions of specific energy calculated using each microdosimetric approach at four different LET points (9.86, 44.3,

195 and 688 keV/µm). The low limit of the horizontal axis was set at 0.01 Gy, which corresponds approximately to the energy from a single ionization (10.9 eV) within the domain [12]. Spectra calculated using the various microdosimetric functions, and different domain geometries within those functions, clearly converge at high LET, where the range of delta rays approaches and falls below that of the domain radii. The difference in the AMF and the KC models is emphasized in the frequency-weighted distributions, particularly at low LETs, where the impact of the lower-energy delta rays is much higher.

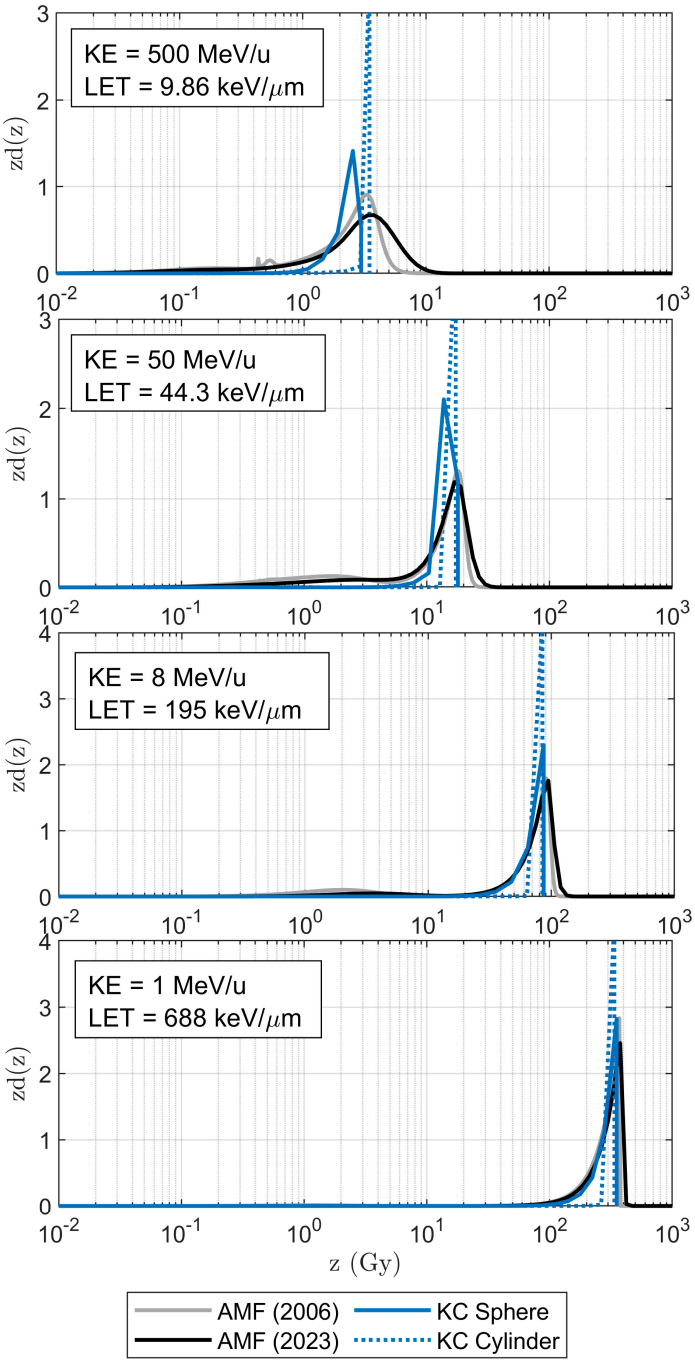


Figure 2. Dose-weighted specific energy spectra calculated as a function of LET for each microdosimetric function and domain geometry.

To qualitatively assess the accuracy of the microdosimetric functions, each of them was compared with spectra measured using a tissue-equivalent proportional counter (TEPC) by Tsuda et al. [28], as shown in Figure 3. The sensitive volume of the TEPC was spherical,

with a radius of 0.36 µm. Subsequently, spectra using each microdosimetric function in Figure 3 were calculated for domain radii of 0.36 and 0.31 µm for spherical and cylindrical geometries, respectively, to achieve equivalent volumes.

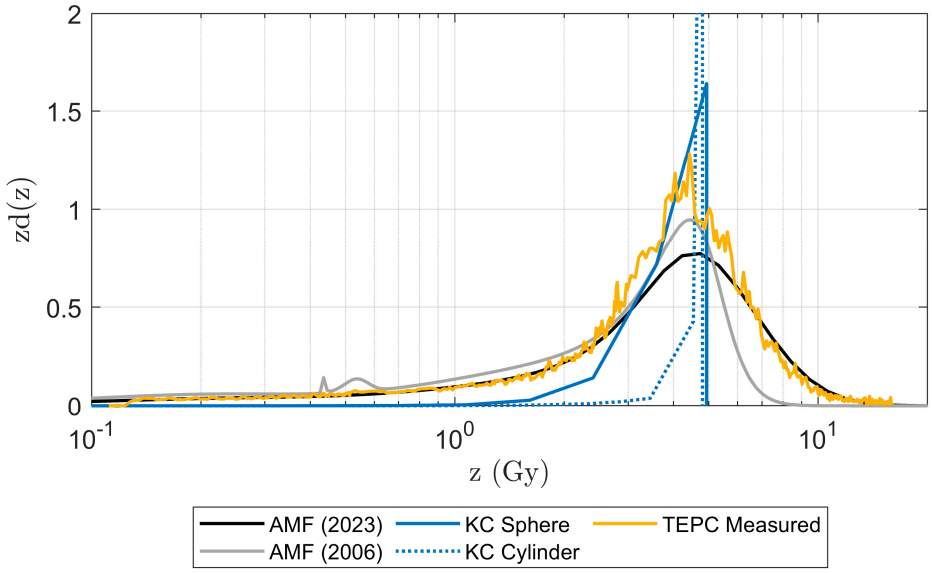


Figure 3. Dose-weighted microdosimetric spectra calculated using each microdosimetric function compared with TEPC-measured data for a 290 MeV/u carbon beam. The radius for the spherical domain geometry is 0.36 µm, consistent with the active volume of the spherical TEPC used by Tsuda et al. [28], while the radius for the cylindrical domains is 0.31 µm to describe an equivalent volume for each geometry.

3.2. Deterministic Microdosimetric Parameters

We next compared $\bar{z}_F$ and $\bar{z}_D$ calculated by each microdosimetric function as a function of LET. We observed a larger spread in $\bar{z}_F$ compared to $\bar{z}_D$ (Figure A8) due to the significant impact of the low-energy delta ray on the frequency-weighted spectra. The $\bar{z}_F$ calculated using the AMFs [11] were notably lower than others due to the substantial delta ray peak that is present in each spectrum in Figure 3. Despite the disagreement in $\bar{z}_F$, the $\bar{z}_D$ computed with the AMF aligned closely with that of the KC model.

The effect of varying domain size on microdosimetric spectra and deterministic microdosimetric parameters was investigated for domain radii ranging from 0.05 to 5.0 µm. The $\bar{z}_F$ values calculated using each microdosimetric function were notably lower for smaller domains than larger domains, which is due to the increased impact of delta ray penumbra seen in spectra calculated for smaller sites. Consequently, due to the weighting of specific energy events, the impact of site size is higher for $\bar{z}_F$ than $\bar{z}_D$.

The $\bar{z}_D$ values calculated using each microdosimetric function and domain geometry combination are shown in Figure 4 for six different domain volumes, with the corresponding radii for each cylinder and spherical domains shown in the legend. This figure additionally shows $\bar{z}_D$ for each microdosimetric function normalized to that of the KC cylinder for the analogous domain size. In this figure, the convergence of the AMF with the KC model can be seen above an LET threshold of about 100 keV/µm. Each AMF shows the same general trend in relation to the KC cylinder, though the 2023 model converges approximately to the predictions of the KC cylinder, while predictions using the 2006 model converge to ~80% those of the KC cylinder.

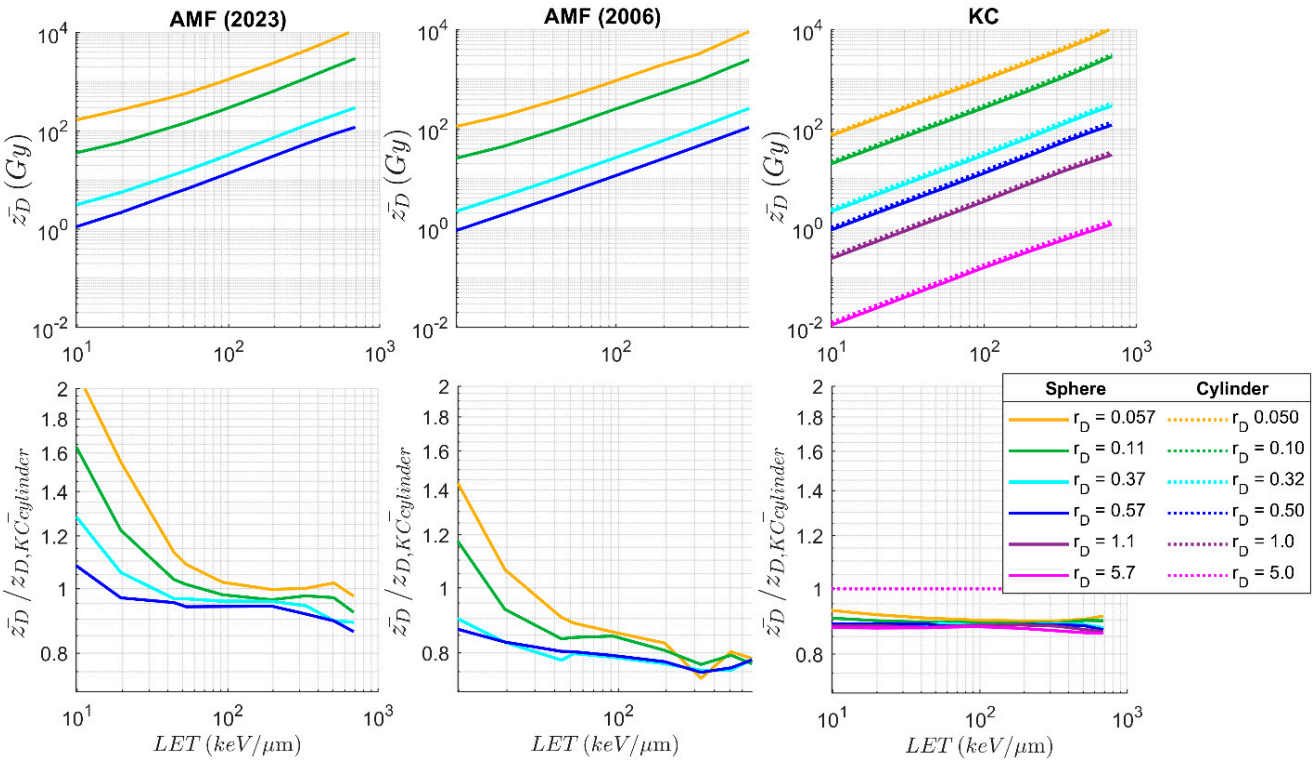


Figure 4. The dose-mean specific energy $\bar{z}_D$ calculated using each microdosimetric function and domain geometry for six different domain volumes on a double logarithmic scale (**top row**) along with $\bar{z}_D$ normalized to that calculated for the KC cylinder for each microdosimetric function and domain geometry on a linear-logarithmic scale (**bottom row**). The radii for each cylinder and sphere corresponding to an equivalent volume between the geometries is shown in the legend (AMF is limited to domain radii ≤ 1 μm).

3.3. Biologic Parameters and RBE

In order to validate our calculations using the KC model, we first reproduced the data published in Inaniwa et al. that implemented the KC model for a cylindrical domain and served as the standard lookup table linking microdosimetry and kinetic energy for ions from hydrogen to carbon [16,17]. These results are shown in Figure A9, overlaid upon digitized results from Inaniwa et al. [16]. Small deviations from the Inaniwa et al. data can be seen for some ions at low energies, below 5 MeV/u, which can be attributed to the difference in LET values used as input to the KC model.

We then determined the sensitivity of this parameter to microdosimetric function and domain geometry by calculating z_D^* using each microdosimetric approach for carbon ions, as shown as a function of LET in Figure 5. Across all four methods of microdosimetric function and domain geometry calculation, the average z_D^* value is shown in Table 1 for each LET point, along with the subsequent spread and standard deviation. Notably, the standard deviation increased steadily from 4.1% to 14% with increasing LET, indicating that sensitivity to the selection of microdosimetric method is of higher consequence at lower beam energies. Within the KC model alone, calculated for different domain geometries, the spread in z_D^* reached 14% at mid-range LET (~150 keV/μm).

To describe the biological effect, the $\mathrm{RBE}_{\mathrm{mMKM}}$ was calculated using the reference parameters previously determined by fitting to in vitro data using the KC model for carbon ions [16]. To compare the sensitivity of RBE to microdosimetric function, $\mathrm{RBE}_{\mathrm{mMKM}}$ was calculated using these same parameters but varying the microdosimetric function used to calculate the mMKM input, z_D^*. To enable a robust comparison, $\mathrm{RBE}_{\mathrm{mMKM}}$ was calculated each for 10% surviving fraction, for a physical dose of 2 Gy, and as the ratio of α_{mMKM}

to α_x to approximate low-dose RBE, as shown in Figure 6. The RBE_{mMKM} using the other microdosimetric functions as input parameters typically followed the same trends as a function of the LET (i.e., reaching a maximum between 100 and 150 keV/µm for carbon and neon ions). The magnitude of RBE_{mMKM} showed a strong dependence on the microdosimetric function, with the most pronounced variations observed for carbon and neon ions at LET values below 300 keV/µm, and for helium ions across all LET ranges.

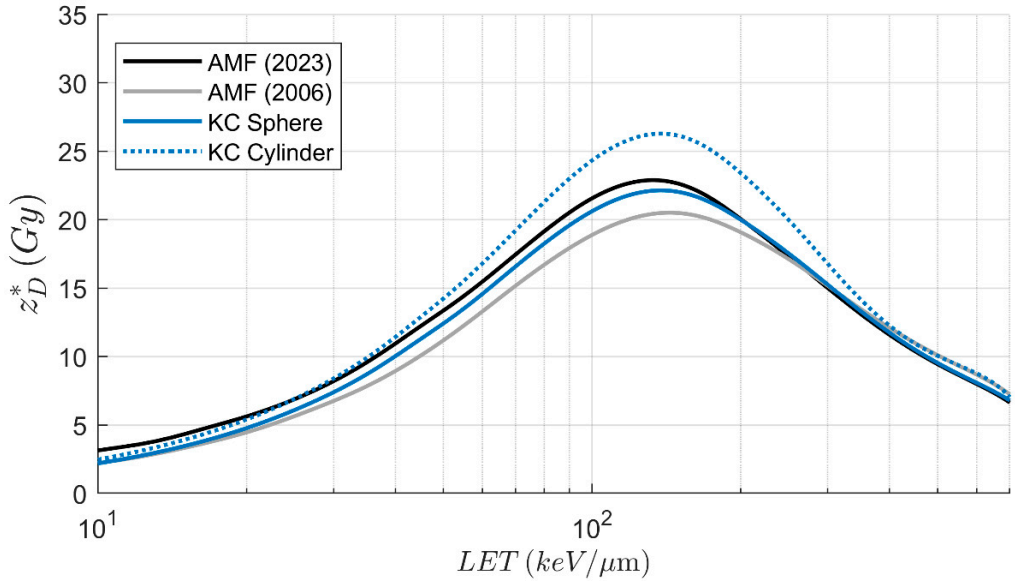


Figure 5. The saturation-corrected dose-mean specific energy, z_D^*, calculated using different microdosimetric functions for cylindrical (dotted line) and spherical (solid line) domains, where applicable, for carbon ions.

Table 1. Mean, spread (max-min), and standard deviation of the z_D^* and $RBE_{10\%}$ calculated for carbon ions using each microdosimetric approach.

LET (keV/µm)	z_D^*			$RBE_{10\%}$		
	Average (Gy)	Spread (Gy)	St. Dev. (%)	Average	Spread	St. Dev. (%)
688	7.14	0.62	4.08%	1.40	1.86%	0.05
508	9.66	0.63	3.49%	1.63	1.99%	0.06
330	14.2	1.30	4.11%	2.07	2.78%	0.13
195	20.9	4.48	9.37%	2.75	7.27%	0.46
92.6	20.6	5.20	10.5%	2.72	8.21%	0.53
44.3	11.4	2.76	10.6%	1.79	6.38%	0.26
19.5	5.07	1.16	10.6%	1.22	3.71%	0.10
9.86	2.50	0.96	18.1%	1.02	3.37%	0.07
8.16	1.93	0.61	13.6%	0.97	2.02%	0.05

In vitro RBE data reported by Furusawa et al. [25] is overlaid with the model calculations for $RBE_{10\%}$ and RBE_{α}. A clear agreement is observed between the Kase implementation of the KC model and the in vitro data, as the biological parameters used to calculate RBE_{mMKM} were those specifically fit by Inaniwa et al. using this microdosimetric function. Overall, the sensitivity of the RBE_{mMKM} increased until an LET of around 100 keV/µm, and then decreased it sharply. At 300 keV/µm and above, the RBE_{mMKM} calculated with each model generally aligned well. Between RBE calculation methods, RBE_{α} were notably more sensitive to microdosimetric function than either the $RBE_{10\%}$ or the RBE_{2Gy}. This lowered sensitivity in $RBE_{10\%}$ and the RBE_{2Gy} is due to the increasing influence of the β parameter

at higher doses, which is constant in the mMKM model and thus impacts all conditions in a similar way.

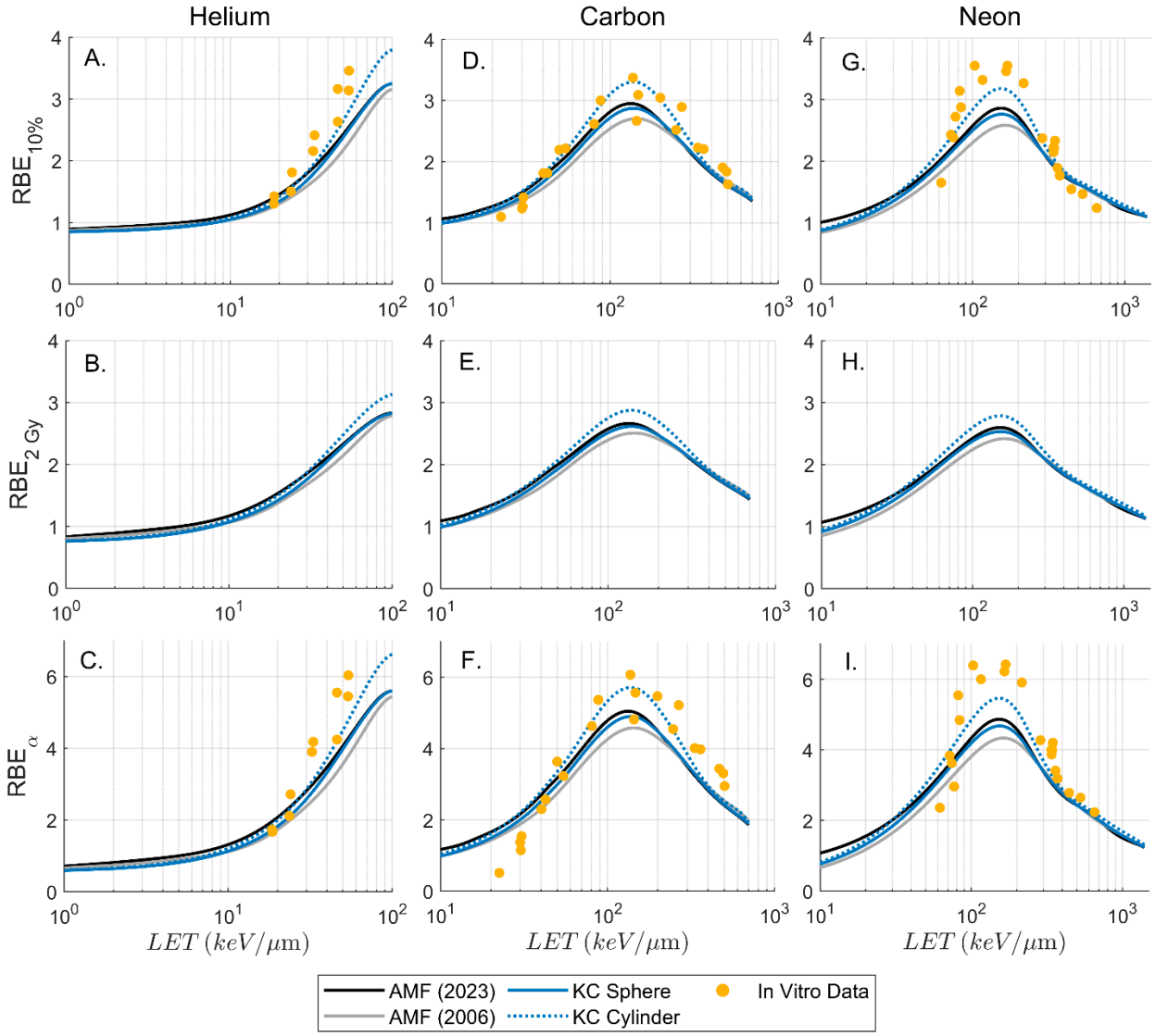


Figure 6. RBE calculated using the mMKM with reference parameters reported by Inaniwa et al. [16] for HSG cells exposed to 200 kVp X-rays using four different microdosimetric inputs. RBE is calculated for three different ions, helium (**A**–**C**), carbon (**D**–**F**), and neon (**G**–**I**), using three different methods: RBE for a surviving fraction of 10% (**A**,**D**,**G**), RBE for a physical dose of 2 Gy (**B**,**E**,**F**), and RBE_{α} (**C**,**H**,**I**) to approximate low-dose RBE. In vitro data published by Furusawa et al. [25] is overlaid for $RBE_{10\%}$ and RBE_{α}.

RBE_{mMKM} calculated using the KC model implemented for cylindrical domain geometries has long served as a reference microdosimetric input to calculations of RBE_{mMKM}, and it is therefore of great interest to determine whether each model examined in this study could approximate the results of the KC cylinder through the use of different mMKM parameters. To verify this, we fit the α_0, R_n, and r_D parameters for each model to those that would reproduce the RBE_{mMKM} calculated using the KC cylinder model, as shown in Figure 7. While the models implemented for spherical geometry were originally calculated using an r_D of 0.37 μm for volume equivalence with the KC cylinder, this value was typically reduced to the same r_D as KC cylinder (0.32 μm), or even below (0.30 μm), in order to achieve reasonably similar RBE values. It is important to note that the parameters shown in Figure 7 do not necessarily represent the best fit to the KC cylinder data but

instead demonstrate that reproducing the KC cylinder results using other models might be feasible.

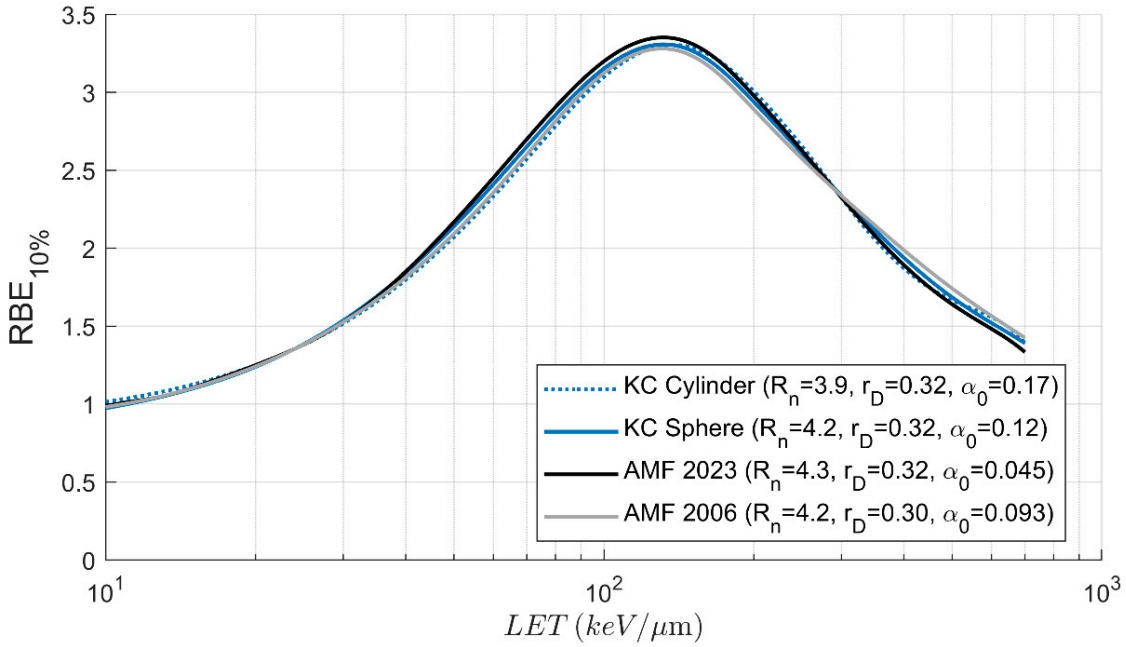


Figure 7. $RBE_{10\%}$ predictions for carbon ions, calculated using each microdosimetric function and domain geometry as input to the mMKM, with the mMKM parameters adjusted to match the RBE_{mMKM} predictions obtained using the KC cylinder model and the original mMKM parameters from Inaniwa et al. [16].

In addition to exploring the effect of microdosimetric function on RBE_{mMKM} for helium and neon ions, we explored the impact of microdosimetric spectra for various ions of the same LET. Here, each function was used to calculate z_D^* and $RBE_{10\%}$ for protons and helium and carbon ions, each at an LET of 9.9 keV/µm (Table A2). Similarly to previous assessments of RBE, HSG cell lines were used as a reference for RBE_{mMKM} calculations. Predictions of each z_D^* and $RBE_{10\%}$ decreased with atomic number for both the AMF and the KC models. The z_D^* and $RBE_{10\%}$ parameters for each proton and helium and carbon ions were additionally recalculated using the fitted parameters determined previously, which were calculated to fit predictions of $RBE_{10\%}$ using each microdosimetric function as an input to RBE_{mMKM} to predictions using the KC cylinder (Table A2). The inconsistency in predictions of RBE_{mMKM} across models for protons and helium ions is evident in this table, resulting from the mMKM parameters being fit to KC cylinder for carbon ions only. This suggests that a robust fitting to multiple ions would be appropriate for a mixed radiation field.

4. Discussion

This study compared multiple methods for calculating microdosimetric spectra, focusing on their treatment of delta-ray contributions beyond the core ion track. Notably, the AMF predicts higher delta-ray contributions at low LET values compared to the KC model. At high LETs, the delta ray contributions in the AMF become practically negligible in the dose-weighted spectra, and the shape of the AMF distribution resembles that of the KC function. Additionally, the AMF produced spectra with higher maximum energy deposition than all other models due to its incorporation of stochastic energy deposition, so that the maximum energy deposition is not simply determined by the product of the average energy deposition (LET) and chord length.

Comparisons between the calculated microdosimetric spectra and the measurements obtained using a TEPC (Figure 4) found that the 2023 AMF demonstrated the closest agreement with the experimental data, outperforming the KC model. This improved alignment is attributed in part to the AMF's more accurate representation of secondary electron contributions. These findings are consistent with a previous study, which benchmarked the 2023 AMF against track structure simulations performed using TOPAS-nBio, a Monte Carlo framework based on Geant4-DNA, and reported excellent agreement [5]. Together, the comparisons with both measured TEPC data and detailed Monte Carlo simulations suggest that the 2023 AMF is a more accurate technique to compute microdosimetric spectra. Moreover, by implementing the KC model for spherical domains in this work, we enabled a direct and geometrically consistent comparison between AMF and KC predictions for the first time.

Domain size also plays a crucial role in interpreting measured spectra, particularly when comparing detectors with fixed domain sizes, such as silicon-on-insulator [9,29–31] and diamond detectors [32,33], to those with variable domain sizes, like gas-filled TEPCs [34–37]. Our findings suggest that as target size increases, differences between microdosimetric parameters calculated using the 2023 AMF and the KC cylinder models become less pronounced, converging when the volume-equivalent targets are large enough to capture most of the secondary electron energy. This has important implications for translating RBE estimates across different detector types and for clinical applications where target size and geometry must be accurately reflected. Microdosimetric quantities can be assessed using lineal energy, described by the quotient of the energy deposited to the domain and the mean chord length of the sensitive volume, rather than specific energy, that relates energy deposited to the mass of the sensitive volume. This is a common approach in practical microdosimetry and can help mitigate some of the differences arising from domain size. An example of this is shown in Figure A10, which depicts the $\bar{z}_D$ and the dose-weighted mean lineal energy, $\bar{y}_D$, calculated using the KC model implemented for a cylindrical domain for six different domain radii.

Beyond the inherent differences among microdosimetric functions, the geometry of the domain employed within these functions also significantly influences the resulting microdosimetric spectra. To isolate this effect, we compared different domain geometries with equivalent volumes. Spherical domains tend to exhibit broader primary peaks due to variations in radiation track lengths, whereas cylindrical domains, with more uniform track lengths, display narrower spectral features. The impact of geometry on z_D^* exceeded 16% between spherical and cylindrical targets, while RBE predictions using the mMKM showed more than a 14% variation.

Noteworthy is the sensitivity of $\mathrm{RBE}_{\mathrm{mMKM}}$ (MF, DG, r_D, R_n, α_0) to microdosimetric function and domain geometry. As seen in Figure 6, $\mathrm{RBE}_{\mathrm{mMKM}}$ varied up to 10% across calculation methods, especially at a lower LET (<400 keV/µm). Interestingly, mMKM parameters, such as r_D, R_n, and α_0, could be adjusted so that the $\mathrm{RBE}_{\mathrm{mMKM}}$ calculated with alternative microdosimetric functions and domain geometries could reasonably reproduce $\mathrm{RBE}_{\mathrm{mMKM}}\left(KC,\ CYL,\ 0.32\ \mu\mathrm{m},\ 3.9\ \mu\mathrm{m},\ 0.172\ \mathrm{Gy}^{-1}\right)$. This is important because years of computational and clinical RBE data rely on the mMKM using the KC model implemented for cylindrical domains and allowing r_D, R_n, and α_0 to be free fitting parameters [16,17,27,38–40]. While this approach is common for the mMKM, it is not applicable for every MKM-based model. Alternative models, such as the Mayo Clinic Florida microdosimetric kinetic model, determine r_D, R_n, and α_0 a priori [15].

To specifically assess how different microdosimetric models and domain geometries influence predicted RBE, we maintained constant values for all mMKM input parameters (including nuclear radius, α_0, and the reference α and β) throughout this study. We em-

ployed a parameter set derived from X-ray data for an HSG cell line, which is commonly utilized in clinical treatment planning systems and has underpinned extensive prior research and clinical outcome analyses. Although this parameter set may not capture the variability across different cell types, leading to uncertainties in absolute RBE values, our analysis concentrates on the relative differences in RBE predictions attributable exclusively to variations in microdosimetric models and domain geometries. Previous studies have investigated the robustness of the mMKM to variations in input parameters [41,42], and Hartzell et al. further explored the influence of cell line variability [42]. These findings reinforce the importance of understanding how modeling assumptions affect RBE predictions. Our results demonstrate that substituting one microdosimetric model or domain geometry for another, even with fixed input parameters, can significantly alter the predicted biological dose. This highlights the need for careful validation when implementing or modifying RBE models in clinical contexts.

5. Conclusions

This study demonstrated the interplay between an RBE model, the approach used for the computation of the microdosimetric spectra, and the geometry of the sensitive volume. The latter two factors were found to affect the RBE in a comparable way to the variation due to RBE model selection itself, which has been a topic of considerable focus in CIRT [43–47]. Therefore, changes in the computation of the microdosimetric spectra necessitate compensatory tuning of mMKM parameters to maintain consistent RBE calculations.

Author Contributions: Conceptualization and methodology, S.H., K.M.F. and A.P.; software and data acquisition, S.H.; formal analysis and writing—original draft preparation, S.H. and A.P.; validation, S.H. and A.P.; resource, funding acquisition, and supervision, K.M.F. and C.J.B.; writing—review and editing, S.H., K.M.F., A.P., T.S., Y.K., C.D., T.F. and C.J.B. All authors have read and agreed to the published version of the manuscript.

Funding: This research received no external funding.

Institutional Review Board Statement: Not applicable.

Informed Consent Statement: Not applicable.

Data Availability Statement: The data presented in this study are available on request from the corresponding author.

Conflicts of Interest: Yuki Kase is employed by B Dot Medical Inc.

Abbreviations

The following abbreviations are used in this manuscript:

α	Linear term of the linear quadratic model of cell survival
α_0	Linear term of the linear quadratic model of cell survival in the case where linear energy transfer approaches 0
AMF	Analytical microdosimetric function
β	Quadratic term of the linear quadratic model of cell survival
CIRT	Carbon ion radiotherapy
DG	Domain geometry
HSG	Human salivary gland
KC	Kiefer–Chatterjee track structure model
LET	Linear energy transfer
MF	Microdosimetric function

mMKM	Modified microdosimetric kinetic model
PHITS	Particle and heavy ion transport code system
RBE	Relative biological effectiveness
RBE_{mMKM}	Relative biological effectiveness calculated using the modified microdosimetric kinetic model
RBE_{α}	Relative biological effectiveness calculated for low doses
$RBE_{10\%}$	Relative biological effectiveness calculated for a surviving fraction of 10%
RBE_{2Gy}	Relative biological effectiveness calculated for a physical dose of 2 Gy
r_D	Radius of a subnuclear domain
R_n	Radius of a cell nucleus
TEPC	Tissue-equivalent proportional counter
$\overline{y}_D$	Dose-mean lineal energy
$\overline{z}_F$	Frequency-mean specific energy
$\overline{z}_D$	Dose-mean specific energy
z_D^*	Saturation-corrected dose-mean specific energy

Appendix A

This appendix describes the implementation of the KC track structure model as a microdosimetric function for both cylindrical and spherical domains. It also details the calculation of microdosimetric parameters using each function implemented in this study and, finally, the calculation of RBE using the mMKM for CIRT.

Appendix A.1. Implementing KC as a Microdosimetric Function

The KC model is an amorphous track structure model that approximates energy deposited in a microscopic volume by defining core and penumbra regions for charged particles [13,14]. The core region is described as a uniform cylinder of high radiation dose with radius R_c concentrated around the direct path of the ion, and the penumbra region extends out to a radius, R_p, with a decreasing dose that is inversely proportional to the square of the distance from the track center, reflecting the diffusion of energy away from the track core due to delta rays with sufficient energy to leave the core region.

For our calculations, we assumed that the particle track enters, or passes by, a thin cylindrical domain (with radius r_D) perpendicular to the circular plane (with area $\pi {r_D}^2$) as seen in Figure A1, which depicts the schematics of the particle hit. According to the KC function, the dose deposited by the track varies as a function of radial distance extending isotropically outward from the particle, shown by the green gradient in Figure A1. The change in kinetic energy within the volume of the target volume was disregarded. As previously done, the height of the cylinder was chosen to be twice the radius of the domain (Figure A1B) [16,17]. For the spherical domain, we implemented the calculations using a stack of thin cylinders, as shown in Figure A1C.

The methods to calculate the dose to the domain are first demonstrated for the cylindrical case. Given the relatively thin nature of the cylinder, we treated this as a 2-D problem involving the intersection of two circles with arbitrary radii, the centers of which are a distance X apart (a dimension referred to as the impact parameter, Figure A1A). Specifically, we assessed the area of the annulus intersecting with the circular domain, the calculation of which is well described in Mathematica and in the literature [48,49]. To define each annulus, we divided the dose deposition from the particle track into concentric circles, each with radius R_i ranging from the core radius to the maximum radius of the penumbra, spaced equally on a logarithmic scale to improve resolution of high-dose regions near the core. The core region was represented by $R_i \leq R_c$, and the penumbra region of steep gradient by $R_c < R_i \leq R_p$.

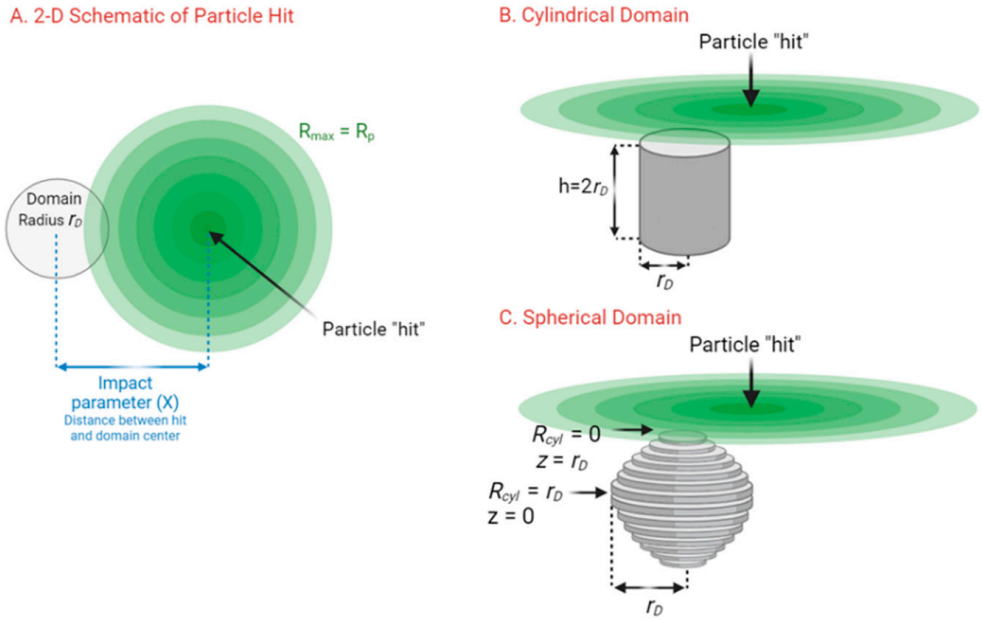


Figure A1. Schematics of a particle hit incident on a microscopic domain. (**A**) shows the 2-D schematic of the particle hit, while (**B**,**C**) depict the particle incident on cylindrical and spherical (approximated with many cylinders) domains, respectively.

For each annulus (the region between concentric circles of R_{i-1} and R_i), the area of intersection with the circular domain was calculated following methods detailed in Appendix A.1. The energy deposited into the domain by that annuli was then calculated by multiplying their annuli intersection area with the height of the cylindrical domain and the dose calculated for that annuli, D_i. The dose was determined using the KC formulas for the core and penumbra regions,

$$D_i = \begin{cases} \frac{0.000125 \cdot Z^{*2}}{{R_i}^2 \beta^2} = \frac{k_p}{{R_i}^2}, & R_c < R_i \leq R_p \\ \left(\frac{1}{\pi {R_c}^2}\right) \cdot \left(\frac{LET \cdot 0.1602}{\rho} - 2\pi k_p \ln\left(\frac{R_p}{R_c}\right)\right), & R_i \leq R_c \end{cases}, \quad \text{(A1)}$$

where ρ represents the density of the domain (fixed at 1 g/cm^3 in this work), Z^* is the effective charge of the ion (calculated with the Barkas expression to account for the gradual electrical neutralization of ions at low velocity [24]), and β is the ion velocity relative to the speed of light. LET is provided in keV/µm, and all radii in micrometers.

Once the total energy deposited into the domain was calculated for each annulus, it was summed over all of the annuli to obtain total energy deposited into the domain from a single particle track with a given impact parameter. A detailed explanation of the energy deposition calculations can be found in Appendix A.2. By dividing the total energy deposited in the domain by the volume of the domain, we obtained the specific energy in the domain as a function of impact parameter, $z(x)$. This analytical approach was consistent with previous works by Kase et al. in 2008 and by Inaniwa et al. in 2010 [16,17].

In extending this problem to a domain of spherical geometry ($r_D = R_{sphere}$), we simply treat the sphere as a number of thin cylinders (NC) of varying radii ($0 < R_{cyl} \leq r_D$) stacked along the z-axis, as shown in Figure A1C. The energy deposited to each cylinder was calculated using the same methods as for the cylindrical domain. The total energy deposited to the spherical domain was summed over all NC thin cylinders and then divided by the sphere's total volume to obtain the specific energy, $z(x)$, for spherical geometries.

For this work, $NC = 100$ was determined to sufficiently represent the spherical geometry, as increasing this number resulted in changes in specific energy of less than 1%.

For each cylindrical and spherical domain, deterministic and biologically weighted microdosimetric parameters, used as inputs to the mMKM RBE model, were calculated analytically by integrating the $z(x)$ spectra, as outlined in Appendix A.4. This entire process of calculating $z(x)$ and subsequent deterministic parameters for each domain geometry is outlined in a decision-making tree in Figure A2. The green loop represents the loop through the annuli of the particle track for a particular thin cylinder and the blue loop represents the loop through the NC stacked cylinders approximating the volume of the sphere ($NC = 100$ for spherical domains and $NC = 1$ for cylindrical domains). Finally, the orange loop represents the loop through the binned values of the impact parameter.

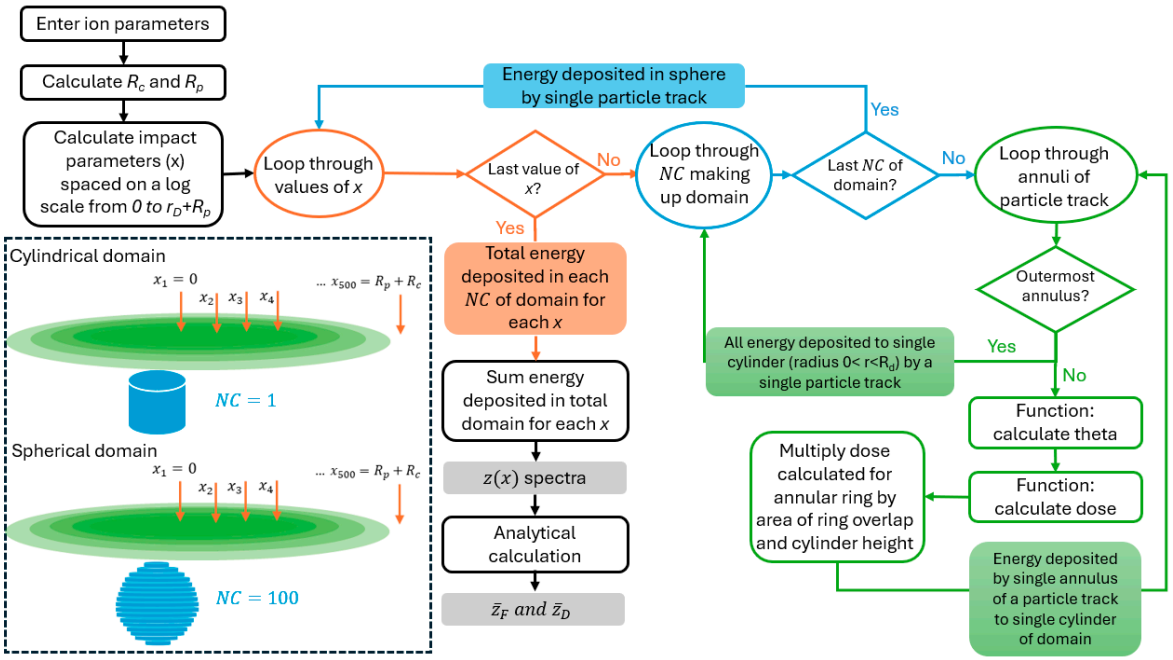


Figure A2. Decision tree for calculation of the z(x) distributions and subsequent deterministic microdosimetric parameters for each cylindrical and spherical domain. The functions "calculate theta" and "calculate dose" mentioned in the green loop through the annuli are described in further detail in Appendices A.2 and A.3.

In order to obtain microdosimetric spectra from the $z(x)$ distributions, we implemented a Monte Carlo simulation where the impact parameter of each particle hit was drawn from a random distribution of points over a disk with radius $r = R_p + r_D$ using MatLab's (R2023a) random number generator [50]. For each impact parameter, the energy deposited in the domain was calculated and binned on a log scale to create a frequency-weighted distribution of energy. The energy axis of this distribution was divided by the mass of the domain to convert the spectra from the frequency of energy deposition to the frequency of specific energy. The frequency of the distribution was then weighted by specific energy to calculate the $zf(z)$ and $zd(z)$ spectra.

Another decision-making tree, shown in Figure A3, depicts the flow of the code that was used for the calculations of the microdosimetric spectra. Only the orange and black loops are different from the analytical decision-making tree shown in Figure A2. Here, the orange loop represents the loop through the x and y coordinates of the sampled particle hits, and the calculations in black represent the process of obtaining microdosimetric spectra.

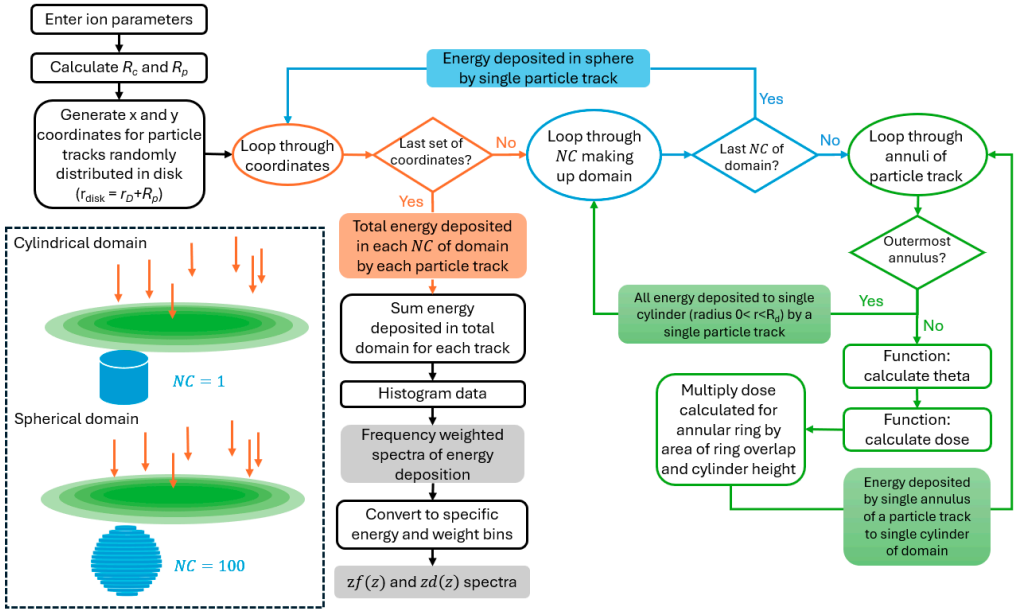


Figure A3. Decision tree for the calculation of microdosimetric spectra using a Monte Carlo approach.

Appendix A.2. Derivation of Overlap of Annulus and Circle

This appendix explains the calculation of a dose to a very thin cylindrical domain from a particle hit using a track structure model, of which the KC is an example. It is assumed that the particle track enters the thin cylinder (Figure A1) perpendicular to the circular plane (area $\pi {r_D}^2$). The dose deposited by the hit varies as a function of radial distance (extending isotropically outward from the particle hit). We reduce this to a 2-D problem of intersection of a circle and an annulus each with known radii; the annulus comprises two concentric circles, and the particle dose deposition is the part of the annulus which overlaps with the circular domain. $N-1$ annuli were defined by dividing the 2-D particle dose deposition into N concentric circles of R_i (where $R_c \leq R_i \leq R_p$). $N = 500$ for the calculations shown.

To calculate the area of overlap of particular annuli with the circular domain, we calculated θ, the angle between the center of the radial dose distribution and the two points of intersection of the dose distribution with the scoring domain. This angle was used to determine the chord length of overlap between the scoring domain and the annulus of dose deposition. There are nine geometric scenarios that were used to calculate θ, following Mathematica's formulism for circle–circle intersections [48].

To implement the calculation of θ into the MATLAB code calculating energy deposited in the domain, a function was written ("calculateTheta"). A decision-making tree describing the function is shown in Figure A4. A table of the formula of theta for the nine scenarios is shown in Table A1.

Table A1. Formula to calculate θ for each scenario described in Figure A4.

Scenario	Formula for θ Calculation
A, B, G, I	$\theta = 2\cos^{-1}\left(\frac{x^2-{r_D}^2+{R_i}^2}{2xR_i}\right)$
C, D, E	$\theta = 2\cos^{-1}\left(\frac{x^2-{r_D}^2+{R_i}^2}{2xR_i}\right) = 0$
F	$\theta = 2\cos^{-1}\left(\frac{x^2-{r_D}^2+{R_i}^2}{2xR_i}\right) = 2\pi$
H	$\theta = 2\pi - 2tan^{-1}\left(\frac{\sqrt{4{R_i}^2x^2-\left(x^2-{r_D}^2+{R_i}^2\right)^2}}{-\left(x^2-{r_D}^2+{R_i}^2\right)}\right)$

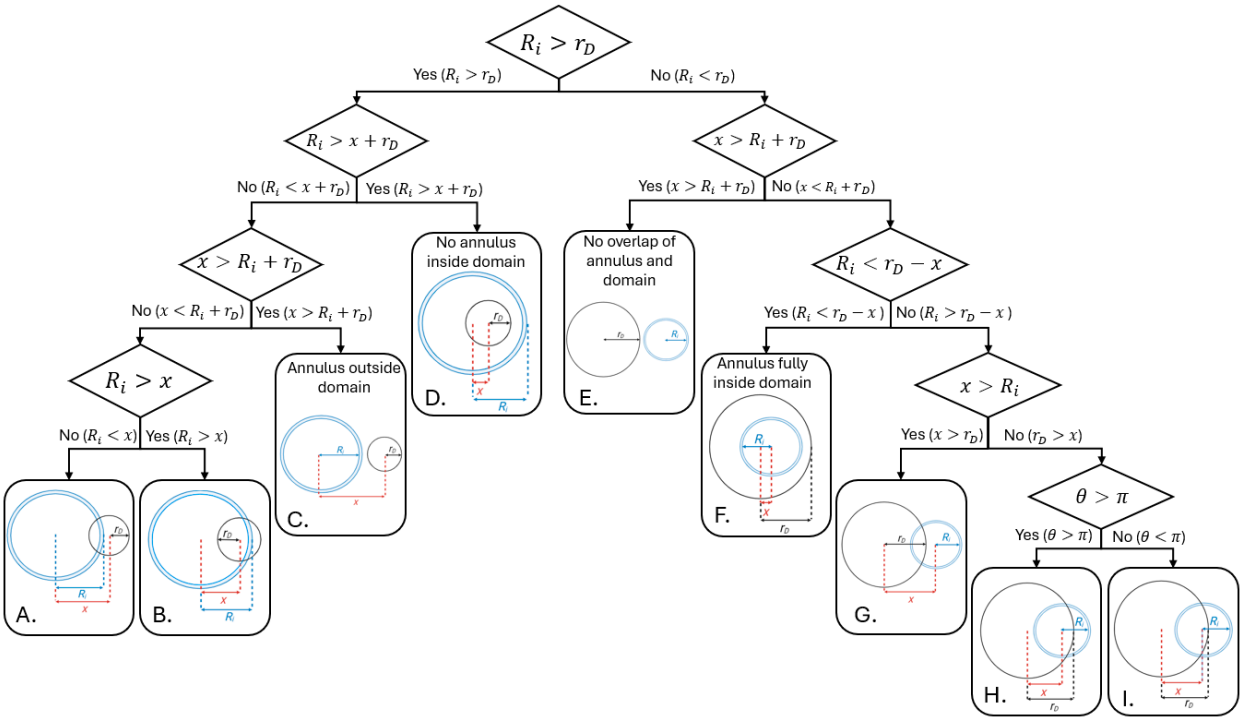


Figure A4. Flow chart of scenarios (**A**–**I**).

Appendix A.3. Energy Deposition in Domain

The methods with which the energy deposition to each cylinder, either constituting the entire domain or part of the domain in the case of spherical geometry, by the particle hit was calculated are as follows. As defined previously, the radial dose dependence of the track structure models was divided into $N = 500$ concentric circles, corresponding to $N - 1$ annuli (each comprising dose deposition between two concentric circles of radii, R_i and R_{i-1}). An example is shown in Figure A5, where the yellow annulus is the annulus for which the energy deposition is being calculated and the red region represents the energy deposition specifically to the domain.

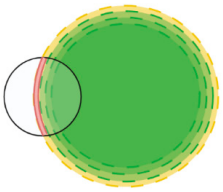


Figure A5. Illustration of the calculation of the energy deposition in the red annulus sector in a domain (black circle) as the product of the energy deposition in the yellow annulus and the ratio of the area of the red annulus sector and the yellow annulus.

The area of an annulus is defined using

$$Area = \pi\left({R_{outer}}^2 - {R_{inner}}^2\right). \tag{A2}$$

If $\Delta r_i = R_i - R_{i-1} \sim 0$, then the area of the annulus is equivalent to the quotient of the circumference of the circle (i.e., $2\pi R_i$) and the thickness of the line (i.e., $\Delta r_i = R_i - R_{i-1}$) so

$$Area = \lim_{\Delta R_i = R_i - R_{i-1} \to 0} 2\pi R_i \, h(R_i - R_{i-1}) \, . \tag{A3}$$

Which is why,

$$Area = \int_{r=0}^{r=R} (length\ of\ circle)dr = \int_{r=0}^{r=R} 2\pi r dr = \pi r^2, \tag{A4}$$

and

$$\frac{dArea}{dr} = \frac{d}{dr}\pi r^2 = 2\pi r. \tag{A5}$$

These two formulas are equivalent for small ΔR_i. The volume of the annuli is then the product of the area of the annuli and the thickness, ($V = 2\pi r \Delta_r h$), where Δ_r is the distance between the two concentric radii.

Therefore, to calculate the energy deposited in the ith annulus of the radial dose dependence, with an outer radius of R_i and a width of $\Delta r_i = R_i - R_{i-1}$, we used the following:

$$D_i\ (R_i) = \frac{d\epsilon(R_i)}{dr} \cdot \Delta r_i \tag{A6}$$

$$D_i\ (R_i) = \frac{d\epsilon(R_i)}{dr} \cdot (R_i - R_{i-1}) \tag{A7}$$

$$D_i\ (R_i) = \frac{\varepsilon_i\ (R_i)}{V_i\ (R_i)} = \frac{\varepsilon_i\ (R_i)}{2\pi R_i\, h(R_i - R_{i-1})} \tag{A8}$$

$$\varepsilon_i = D_i \cdot V_i = D_i \cdot 2\pi R_i\, h(R_i - R_{i-1}) \tag{A9}$$

To calculate the area of overlap of the ith annulus with the domain, we calculated the difference in the area of overlap of the ith circle of radius R_i with the domain ($A_{overlap,\ i}$) and the area of overlap of the $i-1$th circle of radius R_{i-1} with the domain ($A_{overlap,\ i-1}$). The formula for $A_{overlap,\ i}$ (Figure A6) was adapted from Mathematica's calculation of a circular sector [49], where $\theta_{i,d}$ and $\theta_{d,i}$ were calculated using methods described in Appendix A.2.

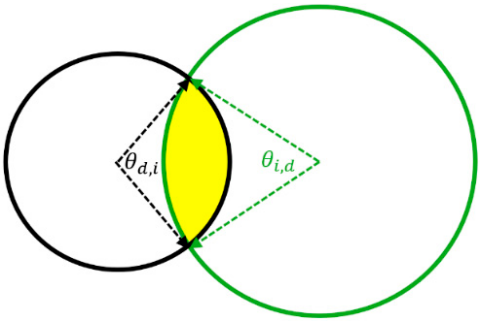


Figure A6. Illustration of the overlap between the domain and the ith annulus.

The formula is as follows:

$$A_{domain\ overlap,\ i} = \frac{1}{2}R_{i,d}^{\ 2}\theta_{i,d} - \frac{1}{2}R_{i,d}^{\ 2}\sin(\theta_{i,d}) + \frac{1}{2}R_{d,i}^{\ 2}\theta_{d,i} - \frac{1}{2}R_{d,i}^{\ 2}\sin(\theta_{d,i}) \tag{A10}$$

$$A_{domain\ overlap,\ i-1} = \frac{1}{2}R_{i-1,d}^{\ 2}\theta_{i-1,d} - \frac{1}{2}R_{i-1,d}^{\ 2}\sin(\theta_{i-1,d}) + \frac{1}{2}R_{d,i-1}^{\ 2}\theta_{d,i-1} - \frac{1}{2}R_{d,i-1}^{\ 2}\sin(\theta_{d,i-1}) \tag{A11}$$

The difference in the overlap areas is then given by

$$\Delta A_{domain\ overlap,i} = A_{overlap,\ i} - A_{overlap,\ i-1} \tag{A12}$$

This can then be used to calculate the energy deposited by the *i*th annulus in the domain using

$$\varepsilon_d(R_i) = \frac{D_i \cdot 2\pi R_i \, h(R_i - R_{i-1}) \cdot \Delta A_{domain\ overlap,i}}{A_{ith\ annulus}} \tag{A13}$$

$$\varepsilon_d(R_i) = \frac{D_i \cdot 2\pi R_i \, h(R_i - R_{i-1}) \cdot \Delta A_{domain\ overlap,i}}{2\pi R_i \, (R_i - R_{i-1})} \tag{A14}$$

$$\varepsilon_d(R_i) = D_i \cdot h \cdot \Delta A_{domain\ overlap,i} \tag{A15}$$

This calculation was repeated for each of the N annuli, and the total energy deposited to the cylinder, making up the partial or entire domain, by the particle hit was summed across all annuli.

Appendix A.4. Calculating Microdosimetric Parameters

After calculating the specific energy for each geometry, expressed as a function of impact parameter for the KC model and as probability density distributions for the AMFs, the next step was to compute the deterministic microdosimetric parameters for each model. Given the differences in output formats between the models, two distinct approaches were employed to calculate the expectation values of specific energy.

For the models based on the computation of microdosimetric distributions (AMFs), the frequency-mean specific energy ($\bar{z}_F$) and dose-mean specific energy ($\bar{z}_D$) were calculated as follows:

$$\bar{z}_F = \int_0^\infty z f(z) dz \tag{A16}$$

and

$$\bar{z}_D = \int_0^\infty z d(z) dz. \tag{A17}$$

By contrast, for the KC approach, these two quantities were assessed by integrating the specific energy with respect to the impact parameter:

$$\bar{z}_F = \int_0^{r_D + R_p} z(x) \cdot 2\pi x dx \tag{A18}$$

and

$$\bar{z}_D = \frac{\int_0^{r_D + R_p} z^2(x) \cdot 2\pi x dx}{\int_0^{r_D + R_p} z(x) \cdot 2\pi x dx}, \tag{A19}$$

where $r_D + R_p$ represents the maximum value of the impact parameter for which the particle can still deposit energy into the domain.

Appendix B

The following appendix includes additional results and analyses that support the findings presented in the main manuscript. While these data were not essential for the primary discussion, they provide further context and may be useful for readers seeking a deeper understanding of specific aspects of the study. The appendix presents supplementary results that further characterize the behavior of each microdosimetric function and domain geometry combination. These include comparative analyses of specific energy metrics ($\bar{z}_F$, $\bar{z}_D$ and z_D^*), validation of the KC model against published data, and $RBE_{10\%}$ predictions under varying model assumptions. Additional tables and figures summarize the variability in RBE estimation, the influence of domain size, and cross-ion comparisons at a matched LET. These figures and tables are referenced throughout the Sections 3 and 4 where appropriate.

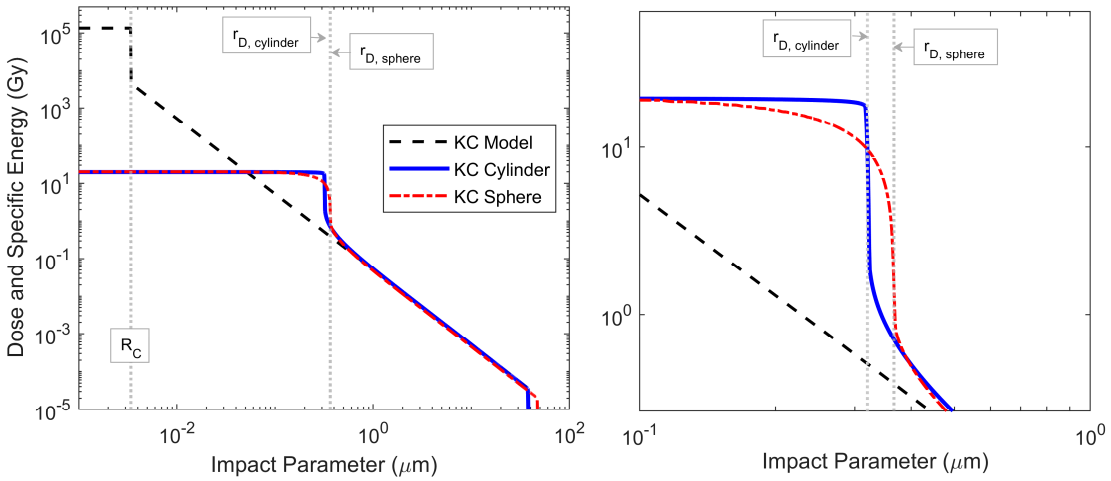


Figure A7. Calculations of dose and specific energy as a function of impact parameter for various implementations of track structure models for a 44 MeV/u carbon ion (LET = 50 keV/µm) on domains with radii of 0.32 µm and 0.37 µm for cylindrical and spherical domains, respectively. A magnification is shown on the right. Vertical lines delineate the core and domain radii on the x-axis. The y-axis represents the dose for the KC model, and specific energy represents that for its microdosimetric implementation.

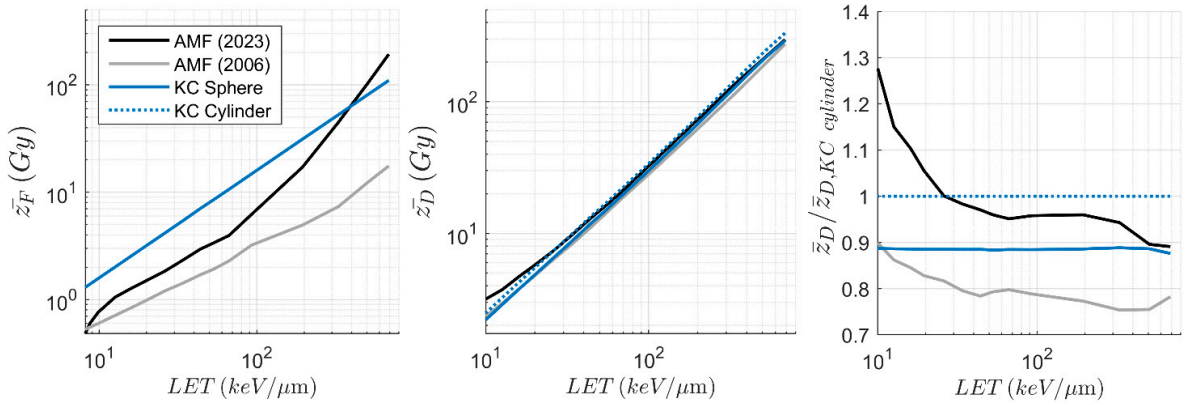


Figure A8. $\bar{z}_F$ (**left**) and $\bar{z}_D$ (**middle**) calculated as a function of LET using each of the microdosimetric functions on a double logarithmic scale. The ratio of $\bar{z}_D$ calculated using each model to that calculated for KC cylinder is shown on a linear scale (**right**).

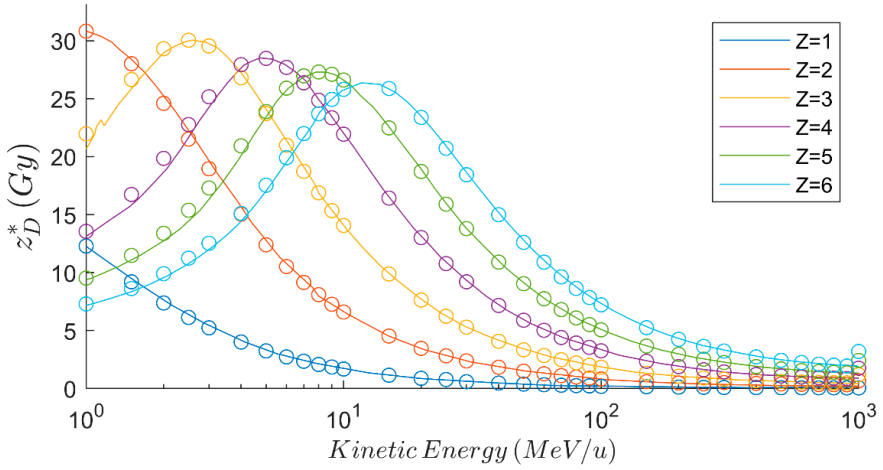


Figure A9. The z_D^* calculated in this study (open circles) overlaid upon digitized data from Inaniwa et al. (lines) for ions with atomic numbers from 1 to 6, serving as validation of our implementation of the KC model for a cylindrical domain.

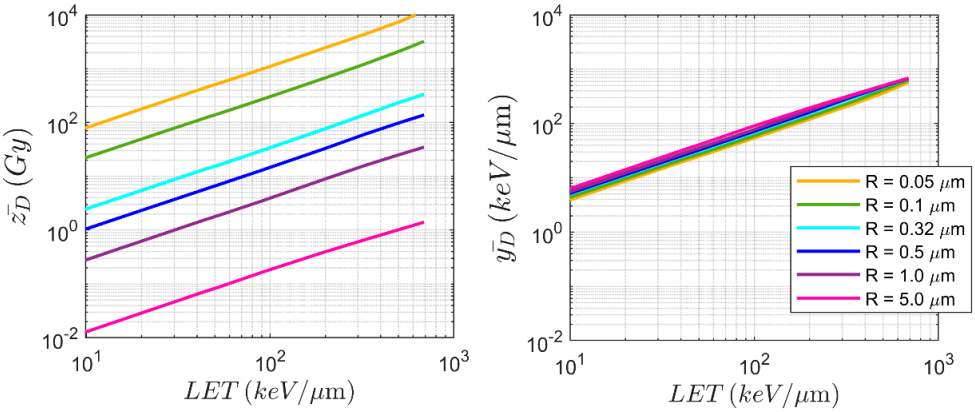


Figure A10. $\bar{z}_D$(**left**) and dose-weighted mean lineal energy, $\bar{y}_D$, (**right**) calculated using the KC model implemented for cylindrical domains using six different domain radii. The y-scale is consistent to emphasize the variability in magnitude of each parameter with domain size.

Table A2. Saturation-corrected specific energy and $RBE_{10\%}$ calculated using the mMKM for each ^{1}H, ^{4}He, and ^{12}C ion at an LET of 9.9 keV/µm.

Ion	Energy (MeV/u)	Parameter	AMF (2023)	AMF (2006)	KC Sphere	KC Cylinder
^{1}H	3.7	z_D^* (Gy) (calculated with Inaniwa 2010 [16] parameters)	4.68	4.21	3.79	4.26
^{4}He	21.6		3.91	2.85	2.92	3.30
^{12}C	500		3.11	2.19	2.18	2.44
^{1}H	3.7	z_D^* (Gy) (calculated with fitted parameters)	6.23	5.28	4.88	4.26
^{4}He	21.6		5.19	3.5	3.77	3.30
^{12}C	500		4.18	2.71	2.79	2.44
^{1}H	3.7	$RBE_{10\%}$ (calculated with Inaniwa 2010 [16] parameters)	1.19	1.15	1.12	1.16
^{4}He	21.6		1.13	1.04	1.05	1.08
^{12}C	500		1.06	1.00	0.99	1.01
^{1}H	3.7	$RBE_{10\%}$(calculated with fitted parameters)	1.15	1.18	1.13	1.16
^{4}He	21.6		1.06	0.995	1.04	1.08
^{12}C	500		0.987	0.979	0.971	1.01

References

1. ICRU. *Microdosimetry. ICRU Report 36*; International Commission on Radiation Units and Measurements: Bethesda, MD, USA, 1983; Volume 36, pp. 35–36.
2. Lindborg, L.; Walker, A. *Microdosimetry: Experimental Methods and Applications*; CRC Press Taylor & Francis Group: Boca Raton, FL, USA, 2017.
3. Liamsuwan, T.; Hultqvist, M.; Lindborg, L.; Uehara, S.; Nikjoo, H. Microdosimetry of proton and carbon ions. *Med. Phys.* **2014**, *41*, 081721. [CrossRef] [PubMed]
4. Bellinzona, V.E.; Attili, A.; Cordoni, F.; Missiaggia, M.; Tommasino, F.; Scifoni, E.; La Tessa, C. Linking microdosimetric measurements to biological effectiveness: A review of theoretical aspects of MKM and other models. *Front. Phys.* **2020**, *8*, 578492. [CrossRef]
5. Hartzell, S.; Parisi, A.; Sato, T.; Beltran, C.J.; Furutani, K.M. Extending TOPAS with an analytical microdosimetric function: Application and benchmarking with nBio track structure simulations. *Phys. Med. Biol.* **2025**, *70*, 105010. [CrossRef] [PubMed]
6. Incerti, S.; Kyriakou, I.; Bernal, M.A.; Bordage, M.C.; Francis, Z.; Guatelli, S.; Ivanchenko, V.; Karamitros, M.; Lampe, N.; Lee, S.B.; et al. Geant4-DNA example applications for track structure simulations in liquid water: A report from the Geant4-DNA Project. *Med. Phys.* **2018**, *45*, e722–e739. [CrossRef]
7. Moeini, H.; Mokari, M. DNA damage and microdosimetry for carbon ions: Track structure simulations as the key to quantitative modeling of radiation-induced damage. *Med. Phys.* **2022**, *49*, 4823–4836. [CrossRef]
8. Conte, V.; Agosteo, S.; Bianchi, A.; Bolst, D.; Bortot, D.; Catalano, R.; Cirrone, G.A.P.; Colautti, P.; Cuttone, G.; Guatelli, S.; et al. Microdosimetry of a therapeutic proton beam with a mini-TEPC and a MicroPlus-Bridge detector for RBE assessment. *Phys. Med. Biol.* **2020**, *65*, 245018. [CrossRef]

9. Tran, L.T.; Bolst, D.; Guatelli, S.; Pogossov, A.; Petasecca, M.; Lerch, M.L.F.; Chartier, L.; Prokopovich, D.A.; Reinhard, M.I.; Povoli, M.; et al. The relative biological effectiveness for carbon, nitrogen, and oxygen ion beams using passive and scanning techniques evaluated with fully 3D silicon microdosimeters. *Med. Phys.* **2018**, *45*, 2299–2308. [CrossRef]
10. Kase, Y.; Kanai, T.; Matsumoto, Y.; Furusawa, Y.; Okamoto, H.; Asaba, T.; Sakama, M.; Shinoda, H. Microdosimetric Measurements and Estimation of Human Cell Survival for Heavy-Ion Beams. *Radiat. Res.* **2006**, *166*, 629–638. [CrossRef]
11. Sato, T.; Watanabe, R.; Niita, K. Development of a calculation method for estimating specific energy distribution in complex radiation fields. *Radiat. Prot. Dosim.* **2006**, *122*, 41–45. [CrossRef]
12. Sato, T.; Matsuya, Y.; Ogawa, T.; Kai, T.; Hirata, Y.; Tsuda, S.; Parisi, A. Improvement of the hybrid approach between Monte Carlo simulation and analytical function for calculating microdosimetric probability densities in macroscopic matter. *Phys. Med. Biol.* **2023**, *68*, 155005. [CrossRef]
13. Kiefer, J.; Straaten, H. A model of ion track structure based on classical collision dynamics. *Phys. Med. Biol.* **1986**, *31*, 1201–1209. [CrossRef]
14. Chatterjee, A.; Schaefer, H.J. Microdosimetric structure of heavy ion tracks in tissue. *Rad. Environ. Biophys.* **1976**, *13*, 215–227. [CrossRef]
15. Parisi, A.; Beltran, C.J.; Furutani, K.M. The Mayo Clinic Florida microdosimetric kinetic model of clonogenic survival: Formalism and first benchmark against in vitro and in silico data. *Phys. Med. Biol.* **2022**, *67*, 185013. [CrossRef]
16. Inaniwa, T.; Furukawa, T.; Kase, Y.; Matsufuji, N.; Toshito, T.; Matsumoto, Y.; Furusawa, Y.; Noda, K. Treatment planning for a scanned carbon beam with a modified microdosimetric kinetic model. *Phys. Med. Biol.* **2010**, *55*, 6721–6737. [CrossRef]
17. Kase, Y.; Kanai, T.; Matsufuji, N.; Furusawa, Y.; Elsässer, T.; Scholz, M. Biophysical calculation of cell survival probabilities using amorphous track structure models for heavy-ion irradiation. *Phys. Med. Biol.* **2008**, *53*, 37–59. [CrossRef]
18. Sato, T.; Iwamoto, Y.; Hashimoto, S.; Ogawa, T.; Furuta, T.; Abe, S.-I.; Kai, T.; Matsuya, Y.; Matsuda, N.; Hirata, Y.; et al. Recent improvements of the particle and heavy ion transport code system—PHITS version 3.33. *J. Nucl. Sci. Technol.* **2024**, *61*, 127–135. [CrossRef]
19. Krämer, M. Calculation of heavy-ion track structure. *Nucl. Instrum. Methods Phys. Res. Sect. B Beam Interact. Mater. At.* **1995**, *105*, 14–20. [CrossRef]
20. ICRU. Key Data for Ionizing-Radiation Dosimetry: Measurement Standards and Applications. *ICRU Report.* 2014. Available online: www.icru.org/report/icru-report-90-key-data-for-ionizing-radiation-dosimetry-measurement-standards-and-applications/ (accessed on 6 May 2024).
21. ICRU. Stopping of ions heavier than Helium. *J. ICRU* **2005**, *73*, iii–viii.
22. Parisi, A.; Beltran, C.J.; Furutani, K.M. The Mayo Clinic Florida Microdosimetric Kinetic Model of Clonogenic Survival: Application to Various Repair-Competent Rodent and Human Cell Lines. *Int. J. Mol. Sci.* **2022**, *23*, 12491. [CrossRef]
23. Parisi, A.; Furutani, K.M.; Sato, T.; Beltran, C.J. Comparative Evaluation of Two Analytical Functions for the Microdosimetry of Ions from 1H to 238U. *Quantum Beam Sci.* **2024**, *8*, 18. [CrossRef]
24. Curtis, S.B. Introduction to Track Structure and z*2/B2. 2016. Available online: https://three.jsc.nasa.gov/articles/Track-Structure-SCurtis.pdf (accessed on 6 May 2024).
25. Furusawa, Y.; Fukutsu, K.; Aoki, M.; Itsukaichi, H.; Eguchi-Kasai, K.; Ohara, H.; Yatagai, F.; Kanai, T.; Ando, K. Inactivation of aerobic and hypoxic cells from three different cell lines by accelerated ^{3}He-, ^{12}C- and ^{20}Ne-ion beams. *Radiat. Res.* **2000**, *154*, 485–496. [CrossRef]
26. Hartzell, S.; Guan, F.; Magro, G.; Taylor, P.; Taddei, P.; Peterson, C.; Kry, S.F. Contribution of nuclear fragmentation to dose and RBE in carbon ion radiotherapy. *J. Radiat. Res.* **2025**, *203*, 96–106. [CrossRef]
27. Inaniwa, T.; Kanematsu, N. Adaptation of stochastic microdosimetric kinetic model for charged-particle therapy treatment planning. *Phys. Med. Biol.* **2018**, *63*, 095011. [CrossRef]
28. Tsuda, S.; Sato, T.; Takahashi, F.; Satoh, D.; Sasaki, S.; Namito, Y.; Iwase, H.; Ban, S.; Takada, M. Systematic Measurement of Lineal Energy Distributions for Proton, He and Si Ion Beams Over a Wide Energy Range Using a Wall-less Tissue Equivalent Proportional Counter. *J. Radiat. Res.* **2012**, *53*, 264–271. [CrossRef]
29. Tran, L.T.; Bolst, D.; James, B.; Pan, V.; Vohradsky, J.; Peracchi, S.; Chartier, L.; Debrot, E.; Guatelli, S.; Petasecca, M.; et al. Silicon 3D Microdosimeters for Advanced Quality Assurance in Particle Therapy. *Appl. Sci.* **2021**, *12*, 328. [CrossRef]
30. Rosenfeld, A.B. Novel detectors for silicon based microdosimetry, their concepts and applications. *Nucl. Instrum. Methods Phys. Res. Sect. A Accel. Spectrometers Detect. Assoc. Equip.* **2016**, *809*, 156–170. [CrossRef]
31. Prieto-Pena, J.; Gómez, F.; Fleta, C.; Guardiola, C.; Pellegrini, G.; Donetti, M.; Giordanengo, S.; González-Castaño, D.M.; Pardo-Montero, J. Microdosimetric Spectra Measurements on a Clinical Carbon Beam at Nominal Therapeutic Fluence Rate With Silicon Cylindrical Microdosimeters. *IEEE Trans. Nucl. Sci.* **2019**, *66*, 1840–1847. [CrossRef]
32. Magrin, G.; Verona, C.; Ciocca, M.; Marinelli, M.; Mastella, E.; Stock, M.; Verona-Rinati, G. Microdosimetric characterization of clinical carbon-ion beams using synthetic diamond detectors and spectral conversion methods. *Med. Phys.* **2019**, *47*, 713–721. [CrossRef]

33. Parisi, G.; Magrin, G.; Verona, C.; Verona-Rinati, G.; Barna, S.; Meouchi, C.; Romano, F.; Schettino, G. On the microdosimetric characterisation of the radiation quality of a carbon-ion beam and the effect of the target volume thickness. *Phys. Med. Biol.* **2024**, *69*, 245003. [CrossRef]
34. Taddei, P.J.; Zhao, Z.; Borak, T.B. A comparison of the measured responses of a tissue-equivalent proportional counter to high energy heavy (HZE) particles and those simulated using the Geant4 Monte Carlo code. *Radiat. Meas.* **2008**, *43*, 1498. [CrossRef]
35. Borak, T.B.; Doke, T.; Fuse, T.; Guetersloh, S.; Heilbronn, L.; Hara, K.; Moyers, M.; Suzuki, S.; Taddei, P.; Terasawa, K.; et al. Comparisons of LET distributions for protons with energies between 50 and 200 MeV determined using a spherical Tissue-Equivalent Proportional Counter (TEPC) and a position-sensitive silicon spectrometer (RRMD-III). *Radiat. Res.* **2004**, *162*, 687–692. [CrossRef]
36. Conte, V.; Colautti, P.; Chiriotti, S.; Moro, D.; Ciocca, M.; Mairani, A. Mini-TEPC Microdosimetric Study of Carbon Ion Therapeutic Beams at CNAO. *EPJ Web Conf.* **2021**, *153*, 01012. [CrossRef]
37. Hartzell, S.; Guan, F.; Taylora, P.; Peterson, C.; Taddei, P.; Kry, S. Uncertainty in tissue equivalent proportional counter assessments of microdosimetry and RBE estimates in carbon radiotherapy. *Phys. Med. Biol.* **2021**, *66*, 155018. [CrossRef]
38. Attili, A.A.-O.; Scifoni, E.A.-O.; Tommasino, F.A.-O. Modelling the HPRT-gene mutation induction of particle beams: Systematicin vitrodata collection, analysis and microdosimetric kinetic model implementation. *Phys. Med. Biol.* **2022**, *67*, 195001. [CrossRef]
39. Manganaro, L.; Russo, G.; Cirio, R.; Dalmasso, F.; Giordanengo, S.; Monaco, V.; Muraro, S.; Sacchi, R.; Vignati, A.; Attili, A. A Monte Carlo approach to the microdosimetric kinetic model to account for dose rate time structure effects in ion beam therapy with application in trreatment planning simulations. *Med. Phys.* **2017**, *44*, 1577–1589. [CrossRef]
40. Magro, G.; Dahle, T.J.; Molinelli, S.; Ciocca, M.; Fossati, P.; Ferrari, A.; Inaniwa, T.; Matsufuji, N.; Ytre-Hauge, K.S.; Mairani, A. The FLUKA Monte Carlo code coupled with the NIRS approach for clinical dose calculations in carbon ion therapy. *Phys. Med. Biol.* **2017**, *62*, 3814–3827. [CrossRef]
41. Dahle, T.J.; Magro, G.; Ytre-Hauge, K.S.; Stokkevåg, C.H.; Choi, K.; Mairani, A. Sensitivity study of the microdosimetric kinetic model parameters for carbon ion radiotherapy. *Phys. Med. Biol.* **2018**, *63*, 225016. [CrossRef]
42. Hartzell, S.; Guan, F.; Magro, G.; Taylor, P.; Peterson, C.; Kry, S. Quantifying sensitivity of carbon RBE models to reference parameter variations. *Radiat. Res.* **2025**. [CrossRef]
43. Mein, S.; Klein, C.; Kopp, B.; Magro, G.; Harrabi, S.; Karger, C.P.; Haberer, T.; Debus, J.; Abdollahi, A.; Dokic, I.; et al. Assessment of RBE-Weighted Dose Models for Carbon Ion Therapy Toward Modernization of Clinical Practice at HIT: In Vitro, in Vivo, and in Patients. *Int. J. Radiat. Oncol. Biol. Phys.* **2020**, *108*, 779–791. [CrossRef]
44. Góra, J.; Grosshagauer, S.; Fossati, P.; Mumot, M.; Stock, M.; Schafasand, M.; Carlino, A. The sensitivity of radiobiological models in carbon ion radiotherapy (CIRT) and its consequences on the clinical treatment plan: Differences between LEM and MKM models. *J. Appl. Clin. Med. Phys.* **2024**, *25*, e14321. [CrossRef]
45. Grosshagauer, S.; Fossati, P.; Schafasand, M.; Carlino, A.; Poljanc, K.; Radakovits, T.; Stock, M.; Hug, E.; Georg, P.; Pelak, M.; et al. Organs at risk dose constraints in carbon ion radiotherapy at MedAustron: Translations between LEM and MKM RBE models and preliminary clinical results. *Radiother. Oncol.* **2022**, *175*, 73–78. [CrossRef] [PubMed]
46. Wang, W.; Huang, Z.; Sheng, Y.; Zhao, J.; Shahnazi, K.; Zhang, Q.; Jiang, G. RBE-weighted dose conversions for carbon ionradiotherapy between microdosimetric kinetic model and local effect model for the targets and organs at risk in prostate carcinoma. *Radiother. Oncol.* **2020**, *144*, 30–36. [CrossRef] [PubMed]
47. Molinelli, S.; Magro, G.; Mairani, A.; Allajbej, A.; Mirandola, A.; Chalaszczyk, A.; Imparato, S.; Ciocca, M.; Fiore, M.R.; Orlandi, E. How LEM-based RBE and dose-averaged LET affected clinical outcomes of sacral chordoma patients treated with carbon ion radiotherapy. *Radiother. Oncol.* **2021**, *163*, 209–214. [CrossRef] [PubMed]
48. Weisstein, E.W. Circle-Circle Intersection. Available online: https://mathworld.wolfram.com/Circle-CircleIntersection.html (accessed on 6 May 2024).
49. Weisstein, E.W. Circular Sector. Available online: https://mathworld.wolfram.com/CircularSector.html (accessed on 6 May 2024).
50. Weisstein, E.W. Disk Point Picking. Available online: https://mathworld.wolfram.com/DiskPointPicking.html (accessed on 6 May 2024).

Disclaimer/Publisher's Note: The statements, opinions and data contained in all publications are solely those of the individual author(s) and contributor(s) and not of MDPI and/or the editor(s). MDPI and/or the editor(s) disclaim responsibility for any injury to people or property resulting from any ideas, methods, instructions or products referred to in the content.